ADVANCED MATERIALS
www.advmat.de

Discovery of Topological Magnetic Textures near Room Temperature in Quantum Magnet $TbMn_6Sn_6$

Zhuolin Li, Qiangwei Yin, Yi Jiang, ZhaoZhao Zhu, Yang Gao, Shouguo Wang, Jun Shen, Tongyun Zhao, Jianwang Cai, Hechang Lei, Shi-Zeng Lin,* Ying Zhang,* and Baogen Shen*

The study of topology in quantum materials has fundamentally advanced the understanding in condensed matter physics and potential applications in next-generation quantum information technology. Recently, the discovery of a topological Chern phase in the spin–orbit-coupled Kagome lattice $TbMn_6Sn_6$ has attracted considerable interest. Whereas these phenomena highlight the contribution of momentum space Berry curvature and Chern gap on the electronic transport properties, less is known about the intrinsic real space magnetic texture, which is crucial for understanding the electronic properties and further exploring the unique quantum behavior. Here, the stabilization of topological magnetic skyrmions in $TbMn_6Sn_6$ using Lorentz transmission electron microscopy near room temperature, where the spins experience full spin reorientation transition between the *a*- and *c*-axes, is directly observed. An effective spin Hamiltonian based on the Ginzburg–Landau theory is constructed and micromagnetic simulation is performed to clarify the critical role of Ruderman–Kittel–Kasuya–Yosida interaction on the stabilization of skyrmion lattice. These results not only uncover nontrivial spin topological texture in $TbMn_6Sn_6$, but also provide a solid basis to study its interplay with electronic topology.

1. Introduction

The discovery of a multitude of novel phenomena such as quantum spin liquid,[1] flat electronic bands,[2–4] topological electronic,[5] and unique magnetic behavior[6,7] in quantum materials with Kagome lattice has made Kagome material an extremely interesting platform. These interesting quantum states appear as a consequence of the nontrivial topology in the electronic band structure and magnetic order, strong electronic correlation, and frustration. Exploring the interplay between electronic band structure and the corresponding magnetism in these materials has led to the discovery of massive Dirac semimetals Fe_3Sn_2,[5] Weyl semimetals Mn_3X (X = Sn, Ge)[8] and $Co_3Sn_2S_2$,[9] which exhibit intrinsic Chern quantum phases, large anomalous Hall effects, and chiral anomalies.[5,10,11] One particularly interesting example is the magnet RMn_6Sn_6 (R = rare-earth elements), which hosts several magnetic orders depending on the interactions between specific R elements and frustrated Mn Kagome lattices.[12–14] The ferrimagnetic structure with the out-of-plane antiparallel arrangement between Tb and Mn moments located at different Kagome sublattice at room temperature has been shown to effectively realize the spinless Haldane model with a topological

Z. Li, Y. Jiang, Z. Zhu, Y. Gao, T. Zhao, J. Cai, Y. Zhang, B. Shen
Beijing National Laboratory for Condensed Matter Physics
Institute of Physics
Chinese Academy of Sciences
Beijing 100190, China
E-mail: zhangy@iphy.ac.cn

Z. Li, Y. Jiang, Z. Zhu, Y. Gao, T. Zhao, J. Cai, Y. Zhang, B. Shen
School of Physical Sciences
University of Chinese Academy of Sciences
Beijing 101408, China

Q. Yin, H. Lei
Laboratory for Neutron Scattering
Beijing Key Laboratory of Opto-Electronic Functional Materials & Micro-Nano Devices
Department of Physics
Renmin University of China
Beijing 100872, China
E-mail: hlei@ruc.edu.cn

The ORCID identification number(s) for the author(s) of this article can be found under https://doi.org/10.1002/adma.202211164.

DOI: 10.1002/adma.202211164

Z. Zhu, Y. Zhang
Songshan Lake Materials Laboratory
Dongguan, Guangdong 523808, China

Y. Gao, S. Wang
School of Materials Science and Engineering
Anhui University
Hefei 230601, China

J. Shen
Department of Energy and Power Engineering
School of Mechanical Engineering
Beijing Institute of Technology
Beijing 100081, China

S.-Z. Lin
Theoretical Division and Center for Integrated Nanotechnologies
Los Alamos National Laboratory
Los Alamos, NM 87545, USA
E-mail: szl@lanl.gov

B. Shen
Ningbo Institute of Materials Technology & Engineering
Chinese Academy of Sciences
Ningbo, Zhejiang 315201, China

Chern band in $TbMn_6Sn_6$.[15–17] Especially, the experimental observation of the edge state and Landau level of the Dirac band in $TbMn_6Sn_6$ represents a key advance in studying quantum-limit Chern topological magnets.[17] However, these phenomena are limited to out-of-plane magnetization at a specific temperature range. On the other hand, several theories have predicted a variety of topological phases by rotating the magnetization in these materials.[18–20] It is interesting to note that the competition between the interlayer interaction and the anisotropy energy between the R and Mn sublattices in RMn_6Sn_6 is temperature dependent, which accounts for the gradual spin reorientation transition (SRT) between out-of-plane and in-plane magnetization near room temperature.[21,22] Therefore, the SRT provides a promising route to tune the electronic band topology in the Kagome materials, such as $TbMn_6Sn_6$, which we will explore in this project.

Meanwhile, it has recently been recognized that the noncollinear magnetization order in the form of proper-screw helix can be stabilized during SRT, which plays a crucial role for the stabilization of the topological magnetic skyrmions.[23–25] The nanometer size and efficient electric-current detection/manipulation/generation behavior endow skyrmions as promising candidates for encoding the information bits with dense integration and high energy efficiency in the next-generation spintronic devices.[26–28] More importantly, theoretical studies hypothesize that the motion of skyrmions in the Kagome magnet can be controlled by the topologically protected edge states.[29] However, the existence of skyrmions in the Kagome quantum magnets remains to be established.

In this work, we directly observe topological magnetic textures in the form of biskyrmion spin configuration via real-space Lorentz transmission electron microscopy (L-TEM) imaging in a centrosymmetric quantum $TbMn_6Sn_6$ magnet. In addition, a periodic magnetic helical order in a broad temperature range of 310–400 K is stabilized as an intermediate state during the continuous magnetization rotation between the *a*- and *c*-axes, clearly highlighting the important role of SRT. Stabilization of the helix and biskyrmions points to competing interactions among frustrated Kagome layers in $TbMn_6Sn_6$, based on which the experimental observations can be described in micromagnetic simulation. The significant topological Hall behavior in correlation with noncollinear spin ordering demonstrates the unique magnetic properties induced by the magnetic field.

2. Results and Discussion

2.1. Direct Visualization of Biskyrmion Generation in $TbMn_6Sn_6$

The pure single-crystal $TbMn_6Sn_6$ was synthesized by the self-flux method, and all X-ray diffraction (XRD) peaks can be indexed with the centrosymmetric *P6/mmm* space group as demonstrated in Note S1 in the Supporting Information. The stacking of the hexagonal Tb layer and the Kagome Mn planes in the sequence of Mn-Tb-Mn-Mn-Tb-Mn along the *c*-axis is schematically shown in **Figure 1**a. It is thought that the magnetic interaction inside the pristine Mn Kagome plane is

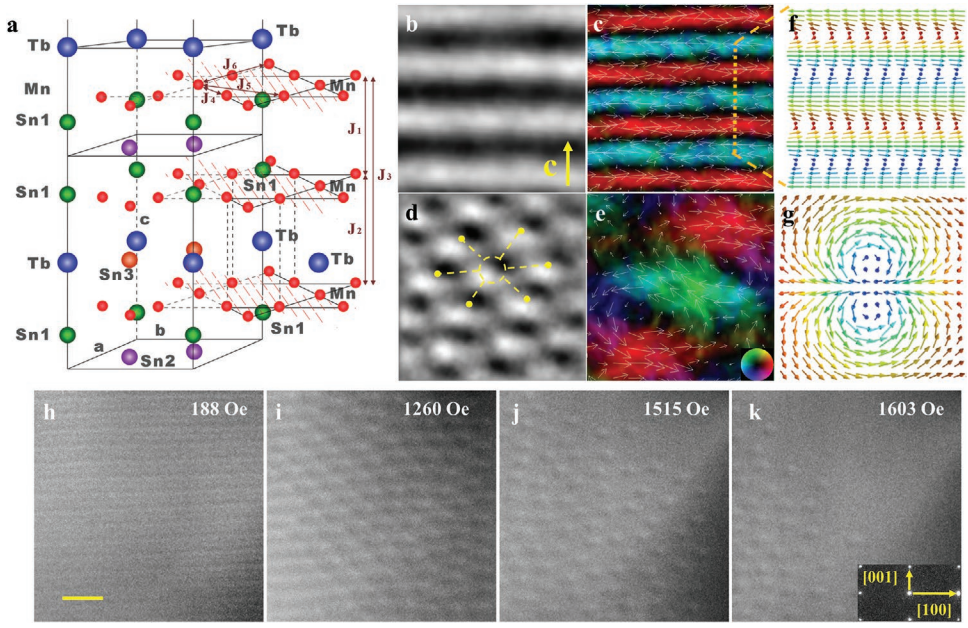

Figure 1. Structures of the helical and biskyrmion domains at 310 K in Kagome $TbMn_6Sn_6$. a) The crystal structure of *P6/mmm* $TbMn_6Sn_6$ with hexagonal R layer and Kagome Mn planes stacked along the *c*-axis in the sequence of Mn-Tb-Mn-Mn-Tb-Mn. The dominant magnetic interactions inside the Kagome Mn-layer and between interlayers are marked out with *J*. b) Phase image of the magnetic helix across the *c*-axis extracted from the L-TEM image. c) The corresponding in-plane magnetic component distribution via TIE analysis. d) Phase image of biskyrmions with a distorted hexagonal lattice at a magnetic field of 1260 Oe. e) The TIE magnetization distribution extracted from the center circle area marked out by yellow dots. f,g) Schematic spin configuration of the helix and biskyrmion. h–k) L-TEM images of domain evolution from the helix to skyrmions and then partially polarized ferromagnetic state via increasing perpendicular magnetic field. The scale bar is 400 nm.

ferromagnetic while the magnetic coupling between Mn-layer and Tb-sublayer is antiferromagnetic.[12–14,30,31] On the contrary, as will be established through the observation of the helix and skyrmion lattice in this work, we demonstrate that the frustrated magnetic interactions should be paid attention.

The ground helical domains and subsequently induced high-density skyrmions under the magnetic field are directly observed along the [010] zone axis at 310 K by L-TEM as shown in Figure 1b–e. The period of helical order and the size of the skyrmion is measured to be about λ = 100 nm. The domain phase image with half-black and half-white contrast in a distorted hexagonal lattice (Figure 1d) is stabilized at the magnetic field of 1260 Oe along the [010] direction. The in-plane magnetization distribution reconstructed by the transport-of-intensity equation (TIE) further identifies the helical (Figure 1c) and biskyrmion spin configuration with opposite magnetic helicities bouncing together (Figure 1e), which is typical in centrosymmetric magnets.[32–34] The corresponding spin configuration is schematically illustrated in Figure 1f,g. The L-TEM images in Figure 1h–k demonstrate the evolution of spin configurations from the helix to skyrmion lattice via applying perpendicular magnetic field at 310 K.

It should be noted that the stripe domains with the helical spin configuration can be recovered after getting rid of the magnetic field. Both the observation of stripe domains and topological biskyrmions adequately confirm the existence of noncollinear spin magnetization in $TbMn_6Sn_6$. The *M*–*H* curve and the L-TEM images at different temperatures consistently demonstrate the equilibrium stabilization of biskyrmions in a temperature region from 310 to 330 K (Note S2, Supporting Information). Moreover, field-cooling (FC) can expand the temperature range of the skyrmion phase to room temperature 300 K, which is more convenient for the application of the topological spin configuration in spintronics (Figure S3, Supporting Information).

The helix magnetization is the building block for the skyrmion lattice, which can be regarded as a superposition of multiple helices. The helix can be stabilized by the Dzyaloshinskii-Moriya interaction (DMI),[23–26] SRT[35] and/or other competing magnetic interactions. The successive domain evolution and magnetization change along the [010] zone axis in **Figure 2** well depict the full magnetization rotation from *a*- to *c*-axis when the temperature is decreased. The temperature-dependent magnetization variation leads to the competition of magnetocrystalline anisotropy for the respective Tb- and Mn-sublattice since the Tb anisotropy decreases more rapidly on heating than that of Mn.[21,22] Therefore, the almost parallel magnetic domain wall along ⟨100⟩ direction indicates an easy in-plane anisotropy along the *a*-axis at 410 K (Figure 2a). When the sample is cooled to about 400 K, some additional stripe domains with helix magnetization structure emerge inside the parallel domains (Figure 2b). Subsequently, the disappearance of in-plane domains and the enhancement of stripe domain contrast indicate a complete canted magnetization state in the form of a proper screw helix (Figure 2c,d). Further decreasing the temperature, the 180° domain wall with magnetization along ⟨001⟩ direction gradually appears below 310 K and occupies the full region at 294 K, as shown in Figure 2e,f. Therefore, the full SRT from the *a*- to *c*-axis with the intermediate canted helix is clearly imaged in our experiment by changing the temperature. It should be noted that the continuous full-spin rotation process occurs in a wide temperature range of about 100 K near room

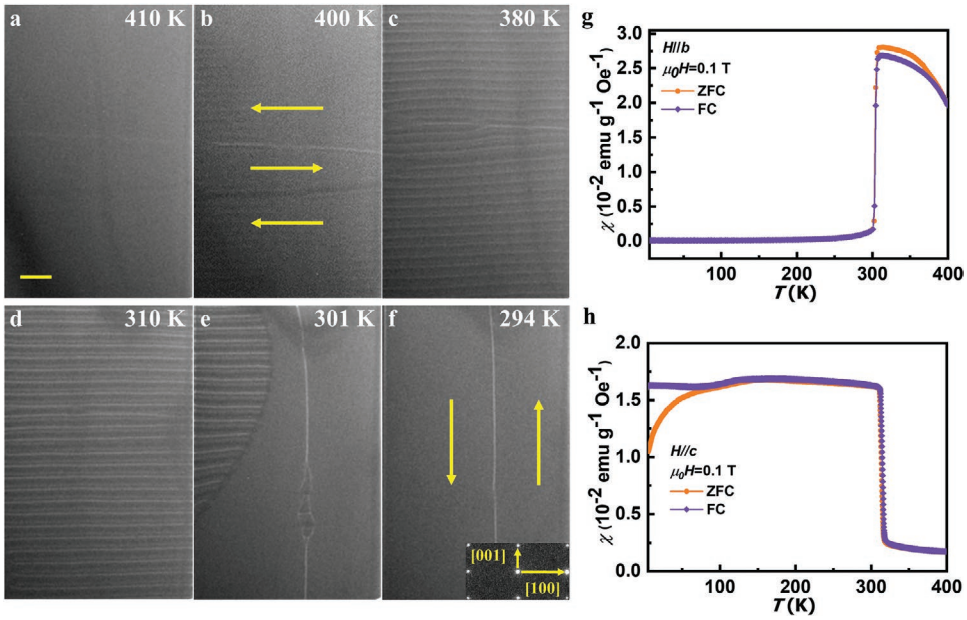

Figure 2. The generation of noncollinear spin magnetization in correlation with temperature-dependent SRT between the *ab*-plane and the *c*-axis in $TbMn_6Sn_6$. a,b) The under-focused L-TEM images showing the magnetic domains with dominant parallel magnetization along the *a*-axis above 400 K. The emergence of stripe domains with helical magnetization at c) 380 and d) 310 K. e,f) The transformation of 180° domain with yellow arrows indicating the dominant magnetic moments along the *c*-axis at 294 K. The electron diffraction pattern in the inset demonstrates the crystal orientation. g,h) Temperature-dependent magnetic susceptibility $\chi(T)$ in zero-field-cooled (ZFC) and field-cooled (FC) modes along the *b*- and *c*-axes, respectively, depicting the switching of the magnetization direction. The scale bar is 400 nm.

temperature. The helical states that generally appear during the SRT have also been studied in YMn_6Sn_6 and $ScMn_6Sn_6$[36–40] both by neutron diffraction studies and theories. Here, the stabilization of helical domains from SRT in $TbMn_6Sn_6$ is directly observed by real-space L-TEM.

This SRT behavior is further confirmed in the temperature-dependent magnetic susceptibility $\chi(T)$ for the $H//b$ and $H//c$ direction, respectively, as shown in Figure 2g,h. The large jumps in $\chi(T)$ curve at T_{sr} = 310 K with opposite changes between the *b*- and *c*-axes, i.e., the susceptibility of the *b*-axis (*c*-axis) decreases (increases) upon lowering the temperature, correspond to the SRT from the *ab* plane at high temperature to the *c*-axis at low temperature.

2.2. Physical Mechanism for Biskyrmion Generation

We construct a theory model to understand the physical mechanism for the stabilization of the topological skyrmion in $TbMn_6Sn_6$. $TbMn_6Sn_6$ is centrosymmetric, and therefore the DM interaction that is responsible for the skyrmion lattice in many chiral magnets is absent. However, the skyrmion lattice can be stabilized by competing magnetic interactions.[41,42] The interaction, known as the Ruderman–Kittel–Kasuya–Yosida (RKKY) interaction, between magnetic moments in the metallic $TbMn_6Sn_6$ is mediated by conduction electrons, which naturally stabilize the helix.[43–47] The momentum-dependent RKKY interaction kernel depends on the details of the Fermi surface and the hybridization function between the conduction electrons and the localized moments.[48–51] Here, we introduce competing interactions with finite interaction range to model the RKKY interaction in $TbMn_6Sn_6$. To take into account the interlayer and intralayer Mn–Mn coupling in a unit cell, we employ and develop the standard object-oriented micromagnetic framework (OOMMF) extensible solver (OXS) modules to construct a micromagnetic system with six types of exchange interactions, including three interlayer exchange interactions (denoted as J_1, J_2, and J_3) and three intralayer exchange interactions (denoted as J_4, J_5, and J_6) as shown in Figure 1a. The energy terms considered in our model can be expressed as the following formula

$$\begin{aligned} E = &-J_1\sum_{\langle ij\rangle}\mathbf{S}_i\cdot\mathbf{S}_j - J_2\sum_{\langle\langle ij\rangle\rangle}\mathbf{S}_i\cdot\mathbf{S}_j - J_3\sum_{\langle\langle\langle ij\rangle\rangle\rangle}\mathbf{S}_i\cdot\mathbf{S}_j \\ &-J_4\sum_{\langle ij\rangle}\mathbf{S}_i\cdot\mathbf{S}_j - J_5\sum_{\langle\langle ij\rangle\rangle}\mathbf{S}_i\cdot\mathbf{S}_j - J_6\sum_{\langle\langle\langle ij\rangle\rangle\rangle}\mathbf{S}_i\cdot\mathbf{S}_j \\ &-K_1\sum_i\left(S_i^c\right)^2 - K_2\sum_i\left(S_i^c\right)^4 - K_3\sum_i\left(S_i^c\right)^6 \\ &-H_b\sum_i S_i^b + \mathrm{E_{DDI}} \end{aligned} \tag{1}$$

The first row represents interlayer interaction along the *z*-axis. The helical order along the *z*-axis is stabilized by appropriate interlayer exchange interactions, which are summarized and displayed in the phase diagram (Note S3, Supporting Information). The effective ferromagnetic interaction J_2 is introduced in our effective Hamiltonian to include the antiferromagnetic interaction between Mn and Tb atoms since only Mn sublattice is considered in our model.[31] It is demonstrated that long-period helix can also be stabilized with proper value of J_2/J_1 and J_3/J_1. The second row represents the intralayer interaction, which determines the wave vectors inside the Kagome plane. Since the skyrmion size in our experiment is much larger than the crystal lattice parameters, we adopted the Ginzburg–Landau description by taking the continuum limit, $E_{kago}^{ex} = \int dr^3[A_1(\nabla_{ab}\mathbf{S})^2 + A_2(\nabla_{ab}^2\mathbf{S})^2]$ in the Kagome plane (Note S4, Supporting Information). The third row describes an easy axis anisotropy along [001] with higher-order terms up to $K_3\sin^6\theta$, which is essential for a better description of field-induced transitions in RMnSn.[22,52] The last row is the Zeeman energy and the dipole–dipole interaction (DDI). Although there have been reports about the skyrmion generation by DDI in centrosymmetric magnets,[53–55] the discussion in Notes S5 and S6 in the Supporting Information reveals that DDI is not the dominant determination for skyrmion generation but only affects the stripe domain period in $TbMn_6Sn_6$.

Here, we focus on the spin in the *x*–*z* plane both in the experiment and in simulation. Because of the competing interaction in the *y*-direction, the spin texture is also modulated along the *y*-direction, but this cannot be simultaneously visualized in L-TEM. Negative value of K_1 is introduced for the simulation of the field-induced magnetic phase transition (based on Figure 1h–k) due to the easy-plane anisotropy above 310 K. Starting from the random magnetic state, skyrmion states with different topological numbers are obtained (listed in **Figure 3**a). Notice that the simulated L-TEM images of skyrmions with topological charge 2 (Figure 3d) are consistent with our experimental results with half-white and half-black contrast. We find that skyrmions with topological charge 1 have the lowest energy in our model while the biskyrmion state is metastable. Generally, a skyrmion with a higher topological number costs more energy,[42] and most known theoretical models support the skyrmion lattice with skyrmion topological charge 1 with very few exceptions.[55,56] We consider the lattice of skyrmion with topological charge 1 in the following discussion. The energy of the helix phase, skyrmion lattice phase, and ferromagnetic phase (FM) is compared in Figure 3f to locate the phase transitions under different magnetic fields in our model. The helix state at zero field is the lowest energy state, which reproduces the observed ground state in Figure 1h. When the magnetic field is increased, the domain evolves into a skyrmion lattice and then to a ferromagnetic phase, which is consistent with the experimental observation (Figure 1i,j). The corresponding Fourier transformation of the helical domain and skyrmion lattice configurations both in simulation and experiment confirm twofold intensity peaks for the helix phase and sixfold intensity peaks for the skyrmions lattice (Figure 3i–l), which agrees with the L-TEM images (Figure 1h,i). The orientation of the lattice in Figure 3j,l differs by 90°, which could be due to the pinning of skyrmion lattice by the boundary of the simulation box because the skyrmion lattice is weakly coupled to the atomic crystal and is easy to be modulated by the boundary. The overall agreement between the simulation and the experimental results highlights the importance of competing RKKY interactions both inside the Kagome plane and between layers in $TbMn_6Sn_6$, and their role in the stabilization of the observed magnetic topological state.

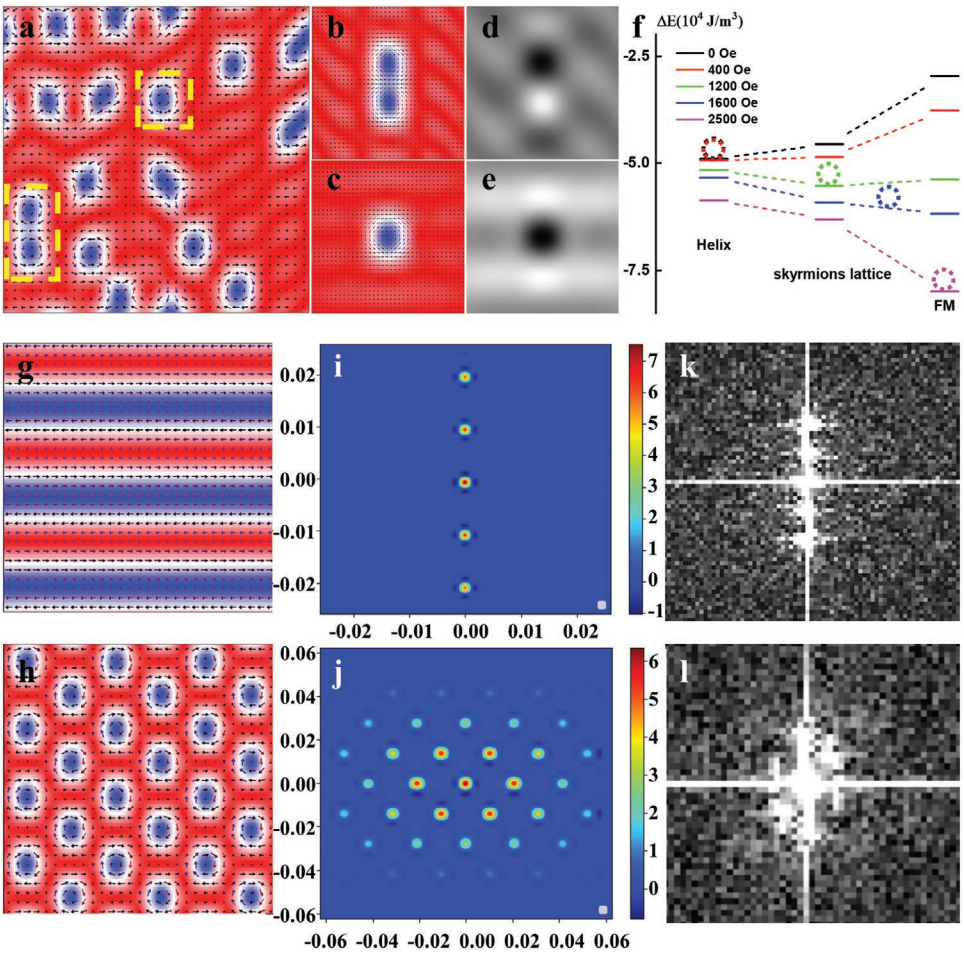

Figure 3. The simulated magnetic states under different magnetic fields based on the experimental results at 310 K. a) A metastable spin configuration obtained by relaxing system from a random initial state in our model using OOMMF. b,c) The spin texture of yellow dot box in (a), which is identified as skyrmions with topological charge equal to b) 2 and c) 1. d,e) The simulated phase image of (b) and (c). f) Comparison of energy of the three magnetic phases under different magnetic fields obtained by OOMMF simulation. The energy reference of ΔE is set as -4.1289×10^8 J m^{-3}. g,h) Spin configurations of the helical domain and skyrmions lattice obtained by OOMMF. The out-of-plane magnetization is represented by red (+m_y) and blue (−m_y), whereas the in-plane magnetization is represented by black arrows. i,j) Fourier transformation of S_z in (g) and (h). The *x*-coordinate represents q_x and *y*-coordinate represents q_y. k,l) Fourier transformation results acquired from the L-TEM pictures of k) the helix and l) biskyrmions lattice in our experiment. The view plane is set as the *x*–*z* plane to be consistent with the experimental condition.

2.3. Electronic Response in Correlation with the Magnetic Transition

The interplay between the topologically nontrivial magnetic texture and electronic structures has attracted considerable attention in the past few years. It is found that the long-range helical order could be linked to the Fermi surface in Weyl semimetal, topological insulators.[57–61] According to theoretical calculations, the topology of skyrmions can give rise to the topology in the electronic band structure and hence the quantized Hall effect when the Fermi surface is parked in the topological gap.[62] The observation of a skyrmion lattice in this work, together with the recent discovery of electronic topology in $TbMn_6Sn_6$, endows Kagome magnets as an ideal platform to study the rich interplay between topology, magnetism, and electronic properties. Here, we measure the Hall conductivity to understand their interplay.

A slice of sample is extracted and manipulated by using focus ion beam (FIB) to realize the *ac*-plane electrical measurement with field applying along the *b*-axis with the sketch shown in **Figure 4**a. The detailed fabrication information can be found in Note S7 in the Supporting Information. The temperature dependence of longitudinal resistivity $\rho_{xx}(T)$ from 5 to 400 K at zero field shows metallic behavior in $TbMn_6Sn_6$ single crystal (Figure 4b). The residual resistivity ratio, defined as ρ_{xx}(400 K)/ρ_{xx}(5 K), is about 44, indicating a high quality of the crystals. It is worth noting that the inflection point at $T_{sr} \sim 310$ K in ρ_{xx}(T) corresponds well with the onset of SRT. At the same time, the metamagnetic transition also has an influence on magnetoresistance (MR, Figure 4c) and the Hall resistivity $\rho_{yx}(\mu_0 H)$ in $TbMn_6Sn_6$ (Figure 4d) for the configuration $I//ac$ and $H//b$. The kinks of $\rho_{yx}(\mu_0 H)$ in Figure 4d indicate a first-order magnetization process induced by applying external magnetic field along the hard axis, which has been previously demonstrated in the neutron diffraction and other physical properties measurements of $TbMn_6Sn_6$.[12,21,22] The corresponding L-TEM images for the filed-induced domain evolution are demonstrated in

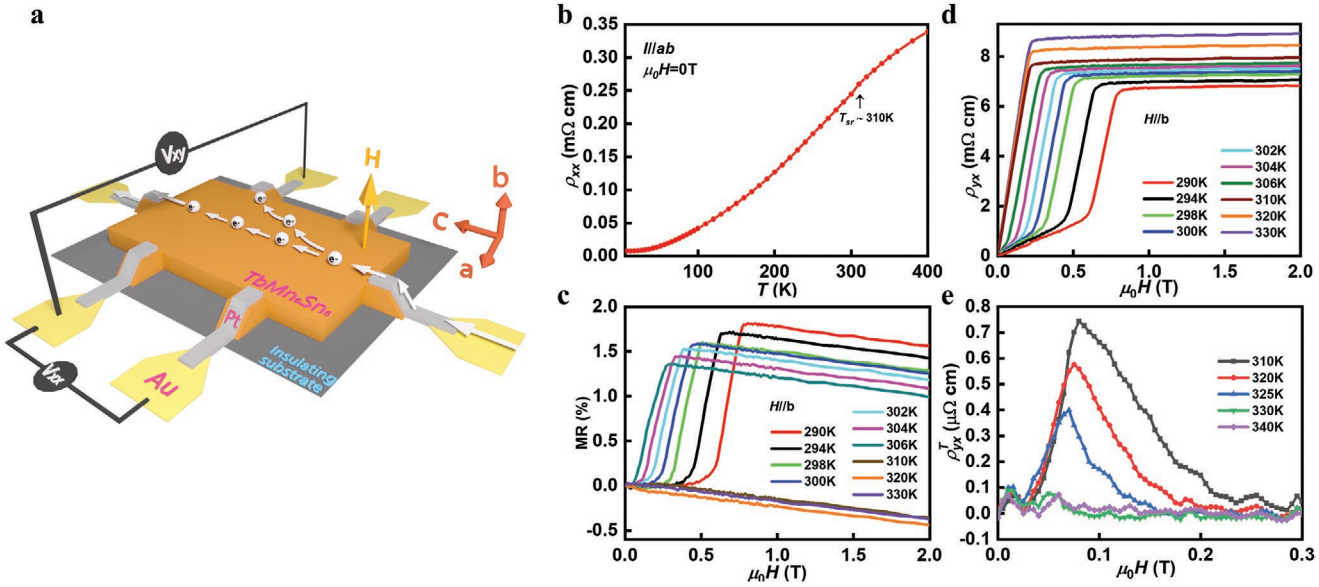

Figure 4. Electrical transport and magnetic transition in $TbMn_6Sn_6$. a) The schematic sketch of $TbMn_6Sn_6$ slice cut by FIB for electrical properties measurement. b) Zero-field $\rho_{xx}(T)$ as a function of temperature. c) Field dependence of MR with $I//ac$ and $H//b$ at various temperatures. d) Field dependence of Hall resistivity $\rho_{yx}(\mu_0 H)$ at different temperatures. e) The extracted topological Hall resistivity $\rho_{yx}^{T}(\mu_0 H)$ at various temperatures.

Note S8 in the Supporting Information. The transition shifts to a lower field region with increasing temperature because of the temperature-dependent magnetization. When $T > T_{sr}$, the magnetic moments rotate to the *ab*-plane and are parallel to the external field applied along the *b*-axis. Then the conventional anomalous Hall conductivity becomes measurable, as will be discussed in detail below. This implies that the magnetic field direction and magnetic structure have significant effects on the electronic structure of $TbMn_6Sn_6$.

In a magnetic system, the total Hall resistivity ρ_{yx} is the sum of three contributions[63,64]

$$\rho_{yx} = \rho_{yx}^{N} + \rho_{yx}^{A} + \rho_{yx}^{T} = R_0 B + S_H \rho_{xx}^{2} M + \rho_{yx}^{T} \quad (2)$$

ρ_{yx}^{N} is the ordinary Hall resistivity due to the Lorentz force generated by magnetic field with a coefficient R_0. ρ_{yx}^{A} denotes the anomalous Hall resistivity determined by M and ρ_{xx}^{n} with a coefficient S_H.[65] For intrinsic anomalous Hall effect, the exponent n is 2, meaning that the anomalous Hall conductivity σ_{yx}^{A} ($\approx \rho_{yx}^{A}/\rho^2$) is in linear relation with M. The last term ρ_{yx}^{T} represents the topological Hall resistivity (THR), originating from noncoplanar spin texture with a nonzero scalar spin chirality. Extracting the first two parts in the above equation, the ρ_{yx}^{T} can be obtained (Figure 4e) and it exists in the temperature range of 310–330 K, where biskyrmions occur under L-TEM observation. The dip in the field dependence of ρ_{yx}^{T} signal reflects the formation and collapse of biskyrmions lattice as the magnetic field is increased. The intensity of ρ_{yx}^{T} and saturation field decreases as temperature is increased and finally vanishes above 330 K. The consistency of temperature and magnetic field ranges uncovers the contribution of biskyrmion lattice to ρ_{yx}^{T} signals. Noticed that the amplitude of THR in Figure 4e is too large for the long magnetic period according to the previous expectations.[63,64] However, it is valid for electron gas coupled to local moments in the strong-coupling regime. For more complex band structure and weak coupling between the local moments and conduction electrons, as in our current case, the topological Hall conductivity depends on microscopic parameters, such as the chemical potential, based on the folded band structure in the presence of skyrmion lattice.[66,67] Although we do not have specific information about the band structure of our magnet, it is quite possible that the THR is large even for a relatively long magnetic period. Further band structure calculations and modeling are required to establish a more precise interplay between the magnetic texture and the electronic band structure.

3. Conclusion

In summary, we have observed real-space skyrmions lattice near room temperature using L-TEM in Kagome magnet $TbMn_6Sn_6$. The skyrmion lattice appears in the low-symmetry *a*–*c* plane when the magnetic field is applied along the *b*-axis owing to the temperature-induced SRT between the *a*- and *c*-axes. This skyrmion lattice is missed in the previous neutron scattering study,[12] where a collinear magnetic order is found, probably due to its long wavelength modulation about λ = 100 nm. Therefore, this work will inspire a more careful study in such materials by using instruments like small angle neutron scattering and L-TEM. We then construct a model that highlights the important roles of the competing RKKY interactions in stabilizing the skyrmion lattice. The discovery of the skyrmion lattice in $TbMn_6Sn_6$ largely enriches the physics by validating Kagome lattice as fertile playgrounds to study the geometry frustration, electronic correlation, and magnetization topology. As already demonstrated in the topological Hall conductivity in this work, the skyrmion lattice has significant effects on the electronic properties and will induce a nontrivial topology in the electronic band structure. Our work not only suggests $TbMn_6Sn_6$ as a promising candidate for spintronics

applications, but also as an interesting platform to study the rich interplay between the real space magnetic topology and momentum space electronic topology.

4. Experimental Section

Sample Synthesis and Structure Characterization: Single crystals of $TbMn_6Sn_6$ were synthesized by self-flux method. High-purity Tb (ingot), Mn (piece), and Sn (grain) were taken in a stoichiometric molar ratio of 1:6:20 and placed in an evacuated quartz tube. The sealed quartz ampoule was heated to 1373 K for 20 h and soaked there for 12 h. Then it was subsequently cooled down to 873 K at 5 K h^{-1}. Finally, the ampoule was taken out from the furnace and decanted with a centrifuge to separate $TbMn_6Sn_6$ crystals from the flux. Single-crystal XRD patterns were acquired using a Bruker D8 X-ray diffractometer with Cu K_α radiation ($\lambda = 0.15418$ nm) at room temperature of 298 K.

Lorentz TEM Measurements: The magnetic domain wall contrast was observed by using a JEOL-dedicated Lorentz TEM (JEOL2100F). Double tilt heating holder (Gatan 652 TA) was used for high-temperature manipulation. The external perpendicular magnetic field was introduced by gradually increasing the objective lens current. The magnetic domain wall contrast at different focus was imaged under the convergent or divergent electron beam, which is introduced by the interaction of electron beam with the in-plane magnetization. To determine the in-plane magnetization distribution of a topological texture, the two sets of images with under- and over-focal lengths were recorded by a charge coupled device camera and then the high-resolution in-plane magnetization distribution map was obtained using commercial software QPt, which enabled to work out phase images and then created the magnetic field images on the basis of the TIE equation. The colors and arrows depict the magnitude and orientation of the in-plane magnetization according to the color wheel. The crystalline orientation for the grain was checked by selected-area electron diffraction. The specimen along [010] zone axis for L-TEM observation was, respectively, prepared via FIB milling.

TIE Analysis: TIE was composed of the following two equations[68]

$$\frac{2\pi}{\lambda}\frac{\partial I(x,y,z)}{\partial z} = -\nabla_{xy}\left(I(x,y,z)\nabla_{xy}\Phi(x,y,z)\right) \tag{3}$$

$$\nabla_{xy}\Phi(x,y,z) = -\frac{e}{\hbar}(\mathbf{M}\times\mathbf{n})t \tag{4}$$

λ is the spectrally weighted mean wavelength of illumination, $\mathbf{n}$ is the unit vector along the beam direction, $\mathbf{M}$ is the magnetization vector, and t is the local sample thickness. The first equation reveals the relationship between phase intensity $I(x,y,z)$ and phase $\Phi(x,y,z)$ and the second equation provides the way to solve in-plane components ($\mathbf{M}\times\mathbf{n}$). To get the information of phase, the under-focused and over-focused pictures were put together in software QPt to find the value of $\frac{\partial I(x,y,z)}{\partial z}$. After resolving the phase, the in-plane magnetization components could be attained consequently.

Micromagnetic Simulation: Micromagnetic simulations were performed using the standard OOMMF[69] extensible solver (OXS) and the OXS extension modules to construct a micromagnetic system with multiple exchange interactions. The exchange energy along the z-axis was calculated using the discrete classical Heisenberg model while the Ginzburg–Landau energy was used in the Kagome plane. Easy-plane anisotropy along [001] axis with higher-order terms, $K_2\sin^4\theta + K_3\sin^6\theta$, was considered in the model, where θ is the angel between spin and [001] axis. Since the magnetization of Tb was always antiparallel with that of Mn, the Mn lattice was only considered in this simulation. The system size in simulation was about $288 \times 150 \times 288$ nm^3 with the periodic boundary condition. The thickness was kept the same as in this experiment since DDI had an impact on the period of helix in this simulation (Note S6, Supporting information). The view plane was set as the xz-plane to be consistent with the experiment. The mesh size was $2 \times 5 \times 2$ nm^3, which was much smaller than the typical exchange length and the skyrmion size, to ensure a balance between numerical accuracy and computational efficiency. After fitting the simulation results with the measured M–H curve and phase diagram obtained by L-TEM at 310 K, the parameters were set as: $J_1 = 26$ meV, $J_2/J_1 = 0.2$, $J_3/J_1 = -0.08386$, $J_4 = 40$ meV, $J_5/J_4 = -0.178$, $J_6/J_4 = -0.08$, $K_1 = -1.8 \times 10^4$ J m^{-3}, $K_2 = 1.5 \times 10^4$ J m^{-3}, $K_3 = -1.6 \times 10^3$ J m^{-4}, $M_s = 201 \times 10^3$ A m^{-1}. In the RMn_6Sn_6 structure, the different Mn–Mn interlayer spacing for Mn-Sn-Mn slab and Mn-R-Mn slab resulted in different interlayer exchange coupling. The lower value of J_2 was based on the previous studies including both theoretical calculations and neutral scattering results.[30,36,37,46]

Transport and Magnetization Characterization: The longitudinal and Hall electrical resistivity were measured simultaneously using a standard five-probe configuration in Quantum Design PPMS-14T. The test specimen along the *ac*-plane with a size of $34 \times 13 \times 2.5$ μm^3 (length × width × thickness) was prepared from a bulk single crystal via FIB (Note S5, Supporting Information). In order to effectively eliminate the influence of voltage probe misalignment, the resistivity was measured in both positive and negative fields. The final longitudinal and Hall resistivity values were obtained by symmetrizing and antisymmetrizing the raw data. Magnetization measurements were performed in Quantum Design MPMS3.

Supporting Information

Supporting Information is available from the Wiley Online Library or from the author.

Acknowledgements

The authors thank Prof. H. M. Weng from Institute of Physics, Chinese Academic of Science for helpful theoretical discussion. This work was supported by the Science Centre of the National Science Foundation of China (grant No. 52088101), the National Natural Science Foundation of China (Nos. 52271195, 11822412, 52130103, 51925605, 11774423, 12274459), the Strategic Priority Research Program of the Chinese Academy of Sciences (grant No. XDB33030100). National Key R&D Program of China (grant no. 2018YFE0202600), Beijing Natural Science Foundation (grant No. Z200005), the Fundamental Research Funds for the Central Universities and Research Funds of Renmin University of China (RUC) (grant Nos. 18XNLG14, 19XNLG13, and 19XNLG17), Beijing National Laboratory for Condensed Matter Physics. The work at LANL was carried out under the auspices of the U.S. DOE NNSA under contract No. 9233218CNA000001 through the LDRD Program, and was performed, in part, at the Center for Integrated Nanotechnologies, an Office of Science User Facility operated for the U.S. DOE Office of Science, under user proposals #2018BU0010 and #2018BU0083.

Conflict of Interest

The authors declare no conflict of interest.

Author Contributions

Y.Z. and B.G.S supervised the project. Q.W.Y. and H.C.L. synthesized the single crystals and carried out structural characterization, transport, and magnetization measurements; Z.Z.Z. and G.Y. helped to prepare the TEM sample and microdevice. Z.L.L. and Y.Z. performed magnetic domain and dynamic behavior experiments via Lorentz TEM. Z.L.L., Q.W.Y., H.C.L., and Y.Z. analyzed the experimental data and plotted the figures; Z.L.L., Y.J., and S.Z.L. did the simulation work; Z.L.L., H.C.L., S.Z.L., and Y.Z. wrote the manuscript after discussing data with J.W.C., T.Y.Z., J.S., S.G.W., B.G.S., and all the authors.

Data Availability Statement

The data that support the findings of this study are available from the corresponding author upon reasonable request.

Keywords

Kagome lattice, quantum magnet $TbMn_6Sn_6$, Ruderman–Kittel–Kasuya–Yosida (RKKY) interaction, topological Hall conductivity, topological skyrmion

Received: November 29, 2022
Revised: February 19, 2023
Published online:

[1] L. Balents, *Nature* **2010**, *464*, 199.
[2] E. Tang, J.-W. Mei, X.-G. Wen, *Phys. Rev. Lett.* **2011**, *106*, 236802.
[3] C. Wu, D. Bergman, L. Balents, S. Das Sarma, *Phys. Rev. Lett.* **2007**, *99*, 070401.
[4] M. Kang, L. Ye, S. Fang, J.-S. You, A. Levitan, M. Han, J. I. Facio, C. Jozwiak, A. Bostwick, E. Rotenberg, M. K. Chan, R. D. Mcdonald, D. Graf, K. Kaznatcheev, E. Vescovo, D. C. Bell, E. Kaxiras, J. Van Den Brink, M. Richter, M. Prasad Ghimire, J. G. Checkelsky, R. Comin, *Nat. Mater.* **2020**, *19*, 163.
[5] L. Ye, M. Kang, J. Liu, F. Von Cube, C. R. Wicker, T. Suzuki, C. Jozwiak, A. Bostwick, E. Rotenberg, D. C. Bell, L. Fu, R. Comin, J. G. Checkelsky, *Nature* **2018**, *555*, 638.
[6] R. Chisnell, J. S. Helton, D. E. Freedman, D. K. Singh, R. I. Bewley, D. G. Nocera, Y. S. Lee, *Phys. Rev. Lett.* **2015**, *115*, 147201.
[7] H. Zhang, X. Feng, T. Heitmann, A. I. Kolesnikov, M. B. Stone, Y.-M. Lu, X. Ke, *Phys. Rev. B* **2020**, *101*, 100405.
[8] H. Yang, Y. Sun, Y. Zhang, W.-J. Shi, S. S. P. Parkin, B. Yan, *New J. Phys.* **2017**, *19*, 015008.
[9] Q. Zhang, S. Okamoto, G. D. Samolyuk, M. B. Stone, A. I. Kolesnikov, R. Xue, J. Yan, M. A. Mcguire, D. Mandrus, D. A. Tennant, *Phys. Rev. Lett.* **2021**, *127*, 117201.
[10] K. Kuroda, T. Tomita, M.-T. Suzuki, C. Bareille, A. A. Nugroho, P. Goswami, M. Ochi, M. Ikhlas, M. Nakayama, S. Akebi, R. Noguchi, R. Ishii, N. Inami, K. Ono, H. Kumigashira, A. Varykhalov, T. Muro, T. Koretsune, R. Arita, S. Shin, T. Kondo, S. Nakatsuji, *Nat. Mater.* **2017**, *16*, 1090.
[11] E. Liu, Y. Sun, N. Kumar, L. Muechler, A. Sun, L. Jiao, S.-Y. Yang, D. Liu, A. Liang, Q. Xu, J. Kroder, V. Süß, H. Borrmann, C. Shekhar, Z. Wang, C. Xi, W. Wang, W. Schnelle, S. Wirth, Y. Chen, S. T. B. Goennenwein, C. Felser, *Nat. Phys.* **2018**, *14*, 1125.
[12] B. Malaman, G. Venturini, R. Welter, J. P. Sanchez, P. Vulliet, E. Ressouche, *J. Magn. Magn. Mater.* **1999**, *202*, 519.
[13] G. Venturini, B. C. E.l Idrissi, B. Malaman, *J. Magn. Magn. Mater.* **1991**, *94*, 35.
[14] D. M. Clatterbuck, K. A. Gschneidner, *J. Magn. Magn. Mater.* **1999**, *207*, 78.
[15] F. D. M. Haldane, *Phys. Rev. Lett.* **1988**, *61*, 2015.
[16] J. Wang, B. Lian, S.-C. Zhang, *Phys. Rev. Lett.* **2015**, *115*, 036805.
[17] J.-X. Yin, W. Ma, T. A. Cochran, X. Xu, S. S. Zhang, H.-J. Tien, N. Shumiya, G. Cheng, K. Jiang, B. Lian, Z. Song, G. Chang, I. Belopolski, D. Multer, M. Litskevich, Z.-J. Cheng, X. P. Yang, B. Swidler, H. Zhou, H. Lin, T. Neupert, Z. Wang, N. Yao, T.-R. Chang, S. Jia, M. Zahid Hasan, *Nature* **2020**, *583*, 533.
[18] S. Nie, Y. Sun, F. B. Prinz, Z. Wang, H. Weng, Z. Fang, X. Dai, *Phys. Rev. Lett.* **2020**, *124*, 076403.
[19] N. Mao, X. Hu, H. Wang, Y. Dai, B. Huang, Y. Mokrousov, C. Niu, *Phys. Rev. B* **2021**, *103*, 195152.
[20] Y. Jin, X.-T. Zeng, X. Feng, X. Du, W. Wu, X.-L. Sheng, Z.-M. Yu, Z. Zhu, S. A. Yang, *Phys. Rev. B* **2021**, *104*, 165424.
[21] G.-H. Guo, H.-B. Zhang, *J. Alloys Compd.* **2008**, *448*, 17.
[22] N. K. Zajkov, N. V. Mushnikov, M. I. Bartashevich, T. Goto, *J. Alloys Compd.* **2000**, *309*, 26.
[23] X. Z. Yu, Y. Onose, N. Kanazawa, J. H. Park, J. H. Han, Y. Matsui, N. Nagaosa, Y. Tokura, *Nature* **2010**, *465*, 901.
[24] S. V. Grigoriev, S. V. Maleyev, A. I. Okorokov, Y. O. Chetverikov, H. Eckerlebe, *Phys. Rev. B* **2006**, *73*, 224440.
[25] X. Z. Yu, N. Kanazawa, Y. Onose, K. Kimoto, W. Z. Zhang, S. Ishiwata, Y. Matsui, Y. Tokura, *Nat. Mater.* **2011**, *10*, 106.
[26] A. Fert, N. Reyren, V. Cros, *Nat. Rev.* **2017**, *2*, 17031.
[27] A. Fert, V. Cros, J. Sampaio, *Nat. Nanotechnol.* **2013**, *8*, 152.
[28] W. Jiang, X. Zhang, G. Yu, W. Zhang, X. Wang, M. Benjamin Jungfleisch, J. E. Pearson, X. Cheng, O. Heinonen, K. L. Wang, Y. Zhou, A. Hoffmann, S. G. E. Te Velthuis, *Nat. Phys.* **2017**, *13*, 162.
[29] M. Pereiro, D. Yudin, J. Chico, C. Etz, O. Eriksson, A. Bergman, *Nat. Commun.* **2014**, *5*, 4815.
[30] S. X. M. Riberolles, T. J. Slade, D. L. Abernathy, G. E. Granroth, B. Li, Y. Lee, P. C. Canfield, B.G. Ueland, L. Ke, R. J. McQueeney, *Phys. Rev. X* **2022**, *12*, 021043.
[31] D. C. Jones, S. Das, H. Bhandari, X. Liu, P. Siegfried, M. P. Ghimire, S. S. Tsirkin, I. I. Mazin, N. J. Ghimire, eprints, arXiv:2203.17246, **2022**.
[32] W. Wang, Y. Zhang, G. Xu, L. Peng, B. Ding, Y. Wang, Z. Hou, X. Zhang, X. Li, E. Liu, S. Wang, J. Cai, F. Wang, J. Li, F. Hu, G. Wu, B. Shen, X.-X. Zhang, *Adv. Mater.* **2016**, *28*, 6887.
[33] L. Peng, Y. Zhang, W. Wang, M. He, L. Li, B. Ding, J. Li, Y. Sun, X.-G. Zhang, J. Cai, S. Wang, G. Wu, B. Shen, *Nano Lett.* **2017**, *17*, 7075.
[34] X. Z. Yu, Y. Tokunaga, Y. Kaneko, W. Z. Zhang, K. Kimoto, Y. Matsui, Y. Taguchi, Y. Tokura, *Nat. Commun.* **2014**, *5*, 3198.
[35] M. He, L. Peng, Z. Zhu, G. Li, J. Cai, J. Li, H. Wei, L. Gu, S. Wang, T. Zhao, B. Shen, Y. Zhang, *Appl. Phys. Lett.* **2017**, *111*, 202403.
[36] G. Venturini, D. Fruchart, B. Malaman, *J. Alloys Compd.* **1996**, *236*, 102.
[37] N. J. Ghimire, R. L. Dally, L. Poudel, D. C. Jones, D. Michel, N. T. Magar, M. Bleuel, M. A. Mcguire, J. S. Jiang, J. F. Mitchell, J. W. Lynn, I. I. Mazin, *Sci. Adv.* **2020**, *6*, eabe2680.
[38] Q. Wang, K. J. Neubauer, C. Duan, Q. Yin, S. Fujitsu, H. Hosono, F. Ye, R. Zhang, S. Chi, K. Krycka, H. Lei, P. Dai, *Phys. Rev. B* **2021**, *103*, 014416.
[39] M. Li, Q. Wang, G. Wang, Z. Yuan, W. Song, R. Lou, Z. Liu, Y. Huang, Z. Liu, H. Lei, Z. Yin, S. Wang, *Nat. Commun.* **2021**, *12*, 3129.
[40] R. L. Dally, J. W. Lynn, N. J. Ghimire, D. Michel, P. Siegfried, I. I. Mazin, *Phys. Rev. B* **2021**, *103*, 094413.
[41] T. Okubo, S. Chung, H. Kawamura, *Phys. Rev. Lett.* **2012**, *108*, 017206.
[42] a) A. O. Leonov, M. Mostovoy, *Nat. Commun.* **2015**, *6*, 8275; b) S.-Z. Lin, S. Hayami, *Phys. Rev. B* **2016**, *93*, 064430.
[43] Y. Fujishiro, N. Kanazawa, Y. Tokura, *Appl. Phys. Lett.* **2020**, *116*, 090501.
[44] M. A. Ruderman, C. Kittel, *Phys. Rev.* **1954**, *96*, 99.
[45] K. Yosida, *Phys. Rev.* **1957**, *106*, 893.
[46] T. A. Kaplan, *Phys. Rev.* **1959**, *116*, 888.
[47] E. V. Rosenfeld, N. V. Mushnikov, *Phys. B* **2008**, *403*, 1898.
[48] S. Hayami, R. Ozawa, Y. Motome, *Phys. Rev. B* **2017**, *95*, 224424.
[49] L. M. Roth, H. J. Zeiger, T. A. Kaplan, *Phys. Rev.* **1966**, *149*, 519.
[50] P. Bruno, C. Chappert, *Phys. Rev. Lett.* **1991**, *67*, 1602.
[51] Y. Akagi, M. Udagawa, Y. Motome, *Phys. Rev. Lett.* **2012**, *108*, 096401.
[52] G. Asti, F. Bolzoni, *J. Magn. Magn. Mater.* **1980**, *20*, 29.
[53] M. Ezawa, *Phys. Rev. Lett.* **2010**, *105*, 197202.

[54] S. A. Montoya, S. Couture, J. J. Chess, J. C. T. Lee, N. Kent, D. Henze, S. K. Sinha, M.-Y. Im, S. D. Kevan, P. Fischer, B. J. Mcmorran, V. Lomakin, S. Roy, E. E. Fullerton, *Phys. Rev. B* **2017**, *95*, 024415.
[55] D. Capic, D. A. Garanin, E. M. Chudnovsky, *Phys. Rev. B* **2019**, *100*, 014432.
[56] R. Ozawa, S. Hayami, Y. Motome, *Phys. Rev. Lett.* **2017**, *118*, 147205.
[57] L. Fu, *Phys. Rev. Lett.* **2009**, *103*, 266801.
[58] X.-Q. Sun, S.-C. Zhang, Z. Wang, *Phys. Rev. Lett.* **2015**, *115*, 076802.
[59] K. M. Döbrich, A. Bostwick, J. L. Mcchesney, K. Rossnagel, E. Rotenberg, G. Kaindl, *Phys. Rev. Lett.* **2010**, *104*, 246401.
[60] S. K. Karna, D. Tristant, J. K. Hebert, G. Cao, R. Chapai, W. A. Phelan, Q. Zhang, Y. Wu, C. Dhital, Y. Li, H. B. Cao, W. Tian, C. R. Dela Cruz, A. A. Aczel, O. Zaharko, A. Khasanov, M. A. Mcguire, A. Roy, W. Xie, D. A. Browne, I. Vekhter, V. Meunier, W. A. Shelton, P. W. Adams, P. T. Sprunger, D. P. Young, R. Jin, J. F. Ditusa, *Phys. Rev. B* **2021**, *103*, 014443.
[61] J. Gaudet, H.-Y. Yang, S. Baidya, B. Lu, G. Xu, Y. Zhao, J. A. Rodriguez-Rivera, C. M. Hoffmann, D. E. Graf, D. H. Torchinsky, P. Nikolić, D. Vanderbilt, F. Tafti, C. L. Broholm, *Nat. Mater.* **2021**, *20*, 1650.
[62] B. Göbel, A. Mook, J. Henk, I. Mertig, *Phys. Rev. B* **2017**, *95*, 094413.
[63] N. Nagaosa, J. Sinova, S. Onoda, A. H. Macdonald, N. P. Ong, *Rev. Mod. Phys.* **2010**, *82*, 1539.
[64] N. Nagaosa, Y. Tokura, *Nat. Nanotechnol.* **2013**, *8*, 899.
[65] C. Zeng, Y. Yao, Q. Niu, H. H. Weitering, *Phys. Rev. Lett.* **2006**, *96*, 037204.
[66] K. Hamamoto, M. Ezawa, N. Nagaosa, *Phys. Rev. B* **2015**, *92*, 115417.
[67] Z. Wang, Y. Su, S.-Z. Lin, C. D. Batista, *Phys. Rev. Lett.* **2020**, *124*, 207201.
[68] M. De Graef, Y. Zhu, *J. Appl. Phys.* **2001**, *89*, 7177.
[69] M. J. Donahue, *OOMMF User's Guide, Version 1.0*, National Institute of Standards and Technology, Gaithersburg, MD **1999**.